Large anisotropy of electron and hole g factors in infrared-emitting InAs/InAlGaAs self-assembled quantum dots

V. V. Belykh,[1,*] D. R. Yakovlev,[1,2] J. J. Schindler,[1] E. A. Zhukov,[1] M. A. Semina,[2] M. Yacob,[3] J. P. Reithmaier,[3] M. Benyoucef,[3] and M. Bayer[1,2]

[1]*Experimentelle Physik 2, Technische Universität Dortmund, D-44221 Dortmund, Germany*
[2]*Ioffe Institute, Russian Academy of Sciences, 194021 St. Petersburg, Russia*
[3]*Institute of Nanostructure Technologies and Analytics (INA), CINSaT, University of Kassel, Heinrich-Plett-Str. 40, D-34132 Kassel, Germany*

(Received 7 December 2015; Revised 11 February 2016; Published 9 March 2016)

arXiv:1512.03544v3 [cond-mat.mes-hall] 12 Mar 2016

A detailed study of the g-factor anisotropy of electrons and holes in $InAs/In_{0.53}Al_{0.24}Ga_{0.23}As$ self-assembled quantum dots emitting in the telecom spectral range of $1.5-1.6$ μm (around 0.8 eV photon energy) is performed by time-resolved pump-probe ellipticity technique using a superconducting vector magnet. All components of the g-factor tensors are measured, including their spread in the quantum dot (QD) ensemble. Surprisingly, the electron g factor shows a large anisotropy changing from $g_{e,x} = -1.63$ to $g_{e,z} = -2.52$ between directions perpendicular and parallel to the dot growth axis, respectively, at an energy of 0.82 eV. The hole g-factor anisotropy at this energy is even stronger: $|g_{h,x}| = 0.64$ and $|g_{h,z}| = 2.29$. On the other hand, the in-plane anisotropies of electron and hole g factors are small. The pronounced out-of-plane anisotropy is also observed for the spread of the g factors, determined from the spin dephasing time. The hole longitudinal g factors are described with a theoretical model that allows us to estimate the QD parameters. We find that the QD height-to-diameter ratio increases while the indium composition decreases with increasing QD emission energy.

PACS numbers: 78.47.D-, 78.67.Hc, 78.55.Cr doi:10.1103/PhysRevB.93.125302

I. INTRODUCTION

Carriers in semiconductors, electrons or holes, are quasiparticles, whose effective spin is strongly modified by the motion in crystal lattice. Consequently, carrier confinement in semiconductor quantum wells (QWs) and quantum dots (QDs) significantly modifies the spin properties. In particular, the QD confinement suppresses the spin-orbit interaction [1], resulting in long spin coherence times [2]. Furthermore, by tailoring the QD potential profile it is possible to adjust electron and hole g factors, which characterize the susceptibility of the spins to a magnetic field. These features make semiconductor QDs attractive systems for manipulating carrier spins both for fundamental and applied research [3].

The carrier confinement in semiconductor heterostructures also changes the band gap energy, i.e., the energy between the lowest conduction band and the highest valence band. This leads to a modification of the *electron g* factor, which can be reasonably well described by the Roth-Lax-Zwerdling relation [4], as demonstrated for CdTe/(Cd,Mg)Te [5] and GaAs/(Al,Ga)As QWs [6, 7] despite its derivation for bulk semiconductors. However, considerable deviations from this relation were found recently in QDs with band gap energy smaller than 1.2 eV [8]. Another consequence of the quantum confinement and the related symmetry reduction in epitaxially grown QWs and QDs is the appearance of the electron g-factor anisotropy, characterized by the difference between the transverse (magnetic field in the sample plane) and longitudinal (magnetic field parallel to the growth axis) g factors $\delta g_e = g_{e\perp} - g_{e||}$. The difference is induced by the modification of the hole states in the valence band (e.g. the splitting of light-hole and heavy-hole states) and their admixture to the electron states in the conduction band. This effect is quite small: the reported $|\delta g_e|$ values for QWs do not exceed $0.1 - 0.2$ [5, 9–14]. Also for standard (In,Ga)As/GaAs QDs emitting at photon energies $E > 1.3$ eV the reported differences do not exceed 0.2 [15–17]. Only for QDs emitting at lower energies indications for a strong anisotropy of the electron g factor were found in electrical [18] and optical [19] measurements. An in-plane electron g-factor anisotropy was also observed, while being rather small with the g-factor difference not exceeding 0.05 [15, 16, 20]. The *hole g* factor, on the other hand, is controlled by the complex spin level structure of the valence band and can vary strongly and nonmonotonically with changing quantum confinement. The out-of-plane and in-plane anisotropy of the hole g factor can be quite large both for QWs and QDs [15, 21–25].

In this paper, we present a comprehensive investigation of the g-factor anisotropy of electrons and holes in $InAs/In_{0.53}Al_{0.24}Ga_{0.23}As$ quantum dots emitting in the telecom spectral range of $1.5-1.6$ μm (around 0.8 eV). A time-resolved pump-probe ellipticity technique employing a superconducting vector magnet allows us to measure all components of the g-factor tensors, including their spread in the QD ensemble. The g-factor anisotropy $|\delta g|$ reaches large values of about 1 for electrons and

* vasilii.belykh@tu-dortmund.de

about 2.8 for holes. We show that the hole longitudinal g factor can be used to estimate key structural parameters of the QDs.

II. EXPERIMENTAL DETAILS

The samples under study were grown by molecular-beam epitaxy on a (001)-oriented InP substrate. The QDs were formed by depositing 5.5 monolayers of InAs on a layer of $In_{0.53}Al_{0.24}Ga_{0.23}As$ also used for capping the dots [8]. The dot density is about 10^{10} cm^{-2}. The diameter and height of the optically active QDs are around 40-50 and 9-13 nm, respectively. Sample A is nominally undoped, and sample B contains a Si δ-doped layer at a distance of 15 nm below the InAs QD layer. The samples mostly differ in the QD emission energies. The QD photoluminescence (PL) spectra of both samples consist of an inhomogeneously broadened line of width ~ 60 meV, centered at ~ 0.81 eV for sample A and at ~ 0.78 eV for sample B [8].

The samples are placed in a vector magnet system consisting of three superconducting split-coils oriented orthogonally to each other. By adjusting the currents in each coil the magnetic field magnitude (up to 3 T) and direction can be varied. The samples are kept at temperature $T = 7-15$ K. A pump-probe technique with polarization sensitivity is implemented to measure the carrier spin dynamics. As laser source we use a NT&C laser system consisting of an Optical Parametric Amplifier (OPA) pumped by a mode-locked Yb:KGW laser operating at 1040 nm [26]. The laser system generates a periodic train (repetition rate 40 MHz) of 300-fs-long pulses at wavelengths tunable in the $1350-4500$ nm ($0.28-0.92$ eV) spectral range. By a pulse shaper, the broad (~ 60 nm) spectrum is shaped down to a width of 20 nm (10 meV) centered at the desired wavelength. Only g-factor energy dependence measurements were done for the laser spectrum shaped to a width of 10 nm (5 meV). The average excitation power was about 10 mW focused to a spot of 50 μm diameter, corresponding roughly to π-pulse excitation as this leads to maximal carrier spin polarization. The laser output is split into the pump and probe beams. The circular-polarized pump pulses induce the carrier spin polarization, whose temporal evolution is probed by measuring the ellipticity of the probe beam, initially linearly polarized, after its transmission through the sample. This method is analogous to measuring the Faraday rotation of the probe beam and provides similar information [27, 28].

In addition, the population dynamics of the optically-injected electron-hole pairs in the QDs is investigated by measuring the differential transmission $\Delta\mathcal{T}/\mathcal{T}$ in a pump-probe experiment. Linearly polarized pump pulses are used to generate the carrier population that is monitored by the linearly polarized probe pulses with variable delay relative to the pump pulses. Pump and probe pulses have the same photon energy and orthogonal linear polarizations to avoid polarization interference.

III. RESULTS AND DISCUSSION

The time dynamics of the spin polarization measured by the pump-probe ellipticity for the magnetic field applied in Voigt geometry (along the sample surface), shows the typical signatures of coherent spin precession, namely, an oscillatory signal about zero level [29] (see the lower curve in Fig. 1). The detailed analysis of this dynamics for sample B was presented in Ref. [8], where it was shown that the oscillations occur at two different frequencies, both of which show a linear dependence on magnetic field. The high-frequency oscillations correspond to the electron spin precession with $|g_{e,x}| \approx 1.6$ for sample A, while the low-frequency oscillations correspond to the hole spin precession with g factor $|g_{h,x}| \approx 0.6$.

We note, that in line with Ref. [8], the linear dependencies of the oscillation frequencies on magnetic field show no offset. According to Ref. [16], this indicates that an exchange interaction of the electron and hole spins is small compared to the Zeeman splitting, so that the oscillations occur on the pure electron and hole spin precession frequencies, while exciton effects can be neglected.

In the following, we describe the experiments in inclined magnetic field using the coordinates xyz, where we chose the z axis along the sample growth direction (001), and the x and y axes in the sample plane, so that the x axis is either along the crystallographic direction (110) or (1$\bar{1}$0). Note, that in the experiment we detect the time evolution of the z projection of the spin polarization, i.e., S_z.

A. Out-of-plane anisotropy

For measurements of the out-of-plane anisotropy of carrier g factors and spin dephasing times, the magnetic field direction was first changed in the xz plane (see inset of Fig. 1). The dynamics of the ellipticity signal at $B = 1$ T for different angles θ between $\mathbf{B}$ and the x axis are shown in Fig. 1. When the angle θ is varied from 0° (Voigt geometry) to 90° (Faraday geometry), the precession frequencies increase, and the amplitude of the oscillating signal becomes smaller up to its disappearance in Faraday geometry. This is accompanied by the appearance of a nonoscillating decaying component, which determines the signal in the Faraday geometry. Also, the decay of the oscillating signal becomes faster with increasing θ. These variations are summarized in quantitative form in Fig. 2 after introduction of the fitting routine.

In the Faraday geometry, the spin dynamics shows only a nonoscillating decay. In this case, the decay of the spin polarization along the z axis, and, correspondingly, along $\mathbf{B}$ is determined by the spin lifetime T_S. This time is contributed by the carrier recombination

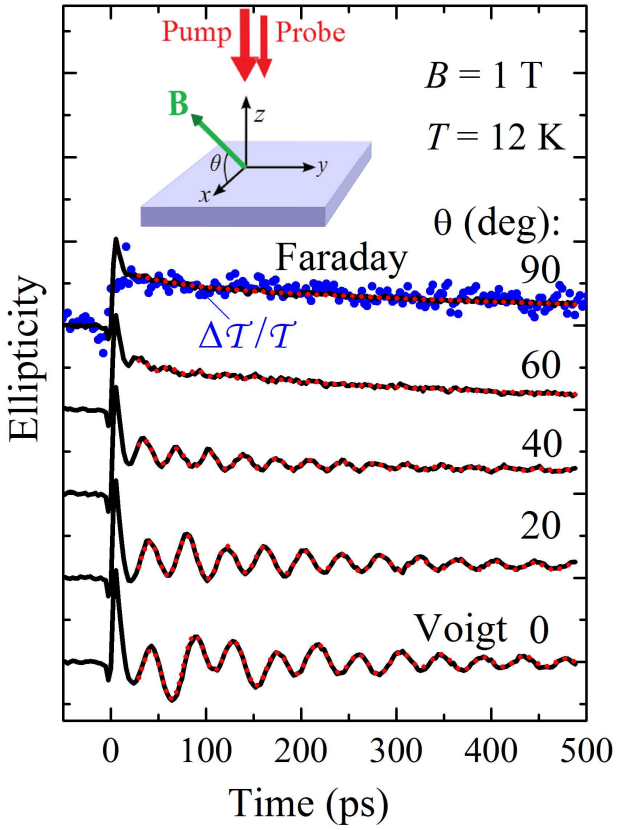

FIG. 1. Dynamics of the ellipticity signal at different angles θ of the magnetic field $B = 1$ T with respect to the sample plane. $\theta = 0^{\circ}$ and $\theta = 90^{\circ}$ correspond to the Voigt and Faraday geometries, respectively. The curves are shifted vertically for clarity. Red dotted lines show fits to the experimental data. Blue solid circles show the dynamics of the differential transmission at $B = 0$ T. The data are shown for the sample A at $T = 12$ K. The central laser photon energy is set to 0.82 eV. Inset shows the experimental geometry.

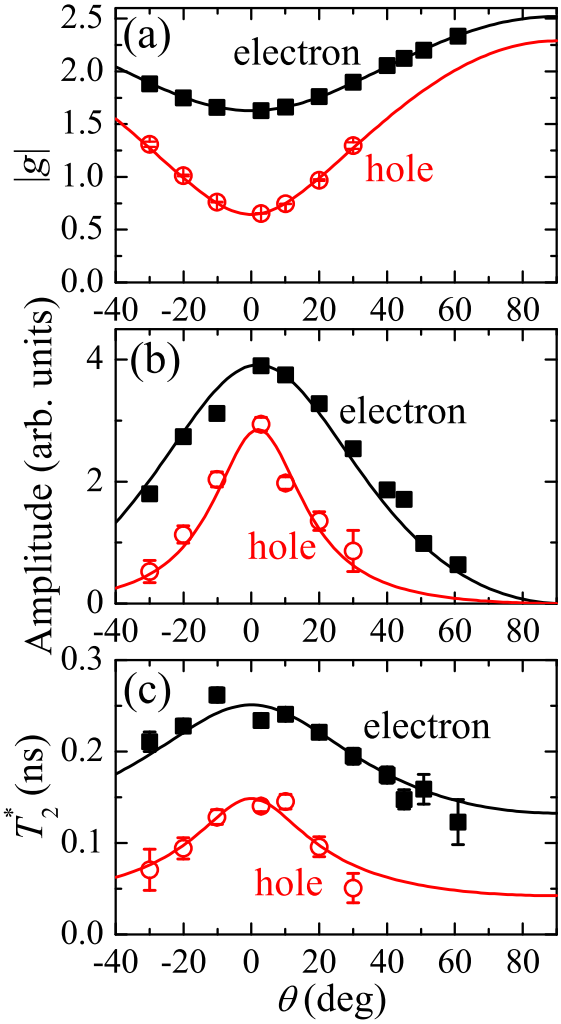

FIG. 2. Dependencies of the g-factor moduli (a), oscillation amplitudes (b) and spin dephasing times (c) on the angle θ between the sample surface and the magnetic field for the electron (solid squares) and hole (open circles) spin precession. Solid lines in panels (a), (b), and (c) show fits to the experimental data with Eqs. (2), (3), and (8), respectively. The data are shown for sample A at $B = 1$ T and $T = 12$ K. The laser photon energy is set to 0.82 eV.

time, $\tau_{\rm rec}$, and the longitudinal spin relaxation time T_1: $1/T_{\rm S} = 1/T_1 + 1/\tau_{\rm rec}$. The T_1 time is usually much longer than the spin coherence time T_2 and the ensemble spin dephasing time T_2^* [30]. As one can see in Fig. 1, the dynamics of the ellipticity signal for $\theta = 90^{\circ}$ coincides with the dynamics of the photocarrier population with $\tau_{\rm rec} \approx 1$ ns measured by the differential transmission experiment (the blue solid circles). Therefore, we conclude that the ellipticity decay time $T_{\rm S} \approx 1$ ns is mainly determined by $\tau_{\rm rec}$. We note that in both samples we do not find indications for a resident carrier population despite the Si-doping in sample B.

The dynamics is fitted with the sum of two damped oscillating functions of type $\cos(\omega t)\exp(-t/T_2^*)$, where t is the time delay between the pump and probe pulses, $\boldsymbol{\omega} = \hat{g}\mu_{\rm B}\mathbf{B}/\hbar$ is the Larmor precession frequency, and $\mu_{\rm B}$ is the Bohr magneton. Note, that the T_2^* times measured in the studied structures are typically shorter than 1 ns, i.e., the decay of the coherent spin dynamics is mainly limited not by the carrier recombination. To account for the nonoscillating component, a double exponential decay was added to the fit. The dependencies of the g-factor values, oscillation amplitudes and dephasing times on the angle θ are shown in Fig. 2 for electron (solid squares) and hole spins (open circles). The error bars in the figure reflect the tolerated deviation of the parameters in the fit of the dynamics. To describe the observed behavior of the spin precession parameters we calculate

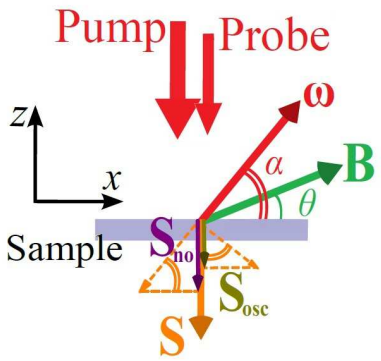

FIG. 3. Schematic representation of the vectors of magnetic field **B**, spin precession frequency $\boldsymbol{\omega}$ and spin polarization **S**. Note, that $\boldsymbol{\omega}$ is not parallel to **B** due to the anisotropy of the g factors. The spin polarization vector is decomposed into the components rotating and nonrotating about $\boldsymbol{\omega}$. In turn, the projections of these components on the probe beam direction (z axis) $\mathbf{S}_{\rm osc}$ and $\mathbf{S}_{\rm no}$ determine the amplitudes of the oscillating and nonoscillating components of the ellipticity signal.

the vector of the Larmor precession frequency:

$$\begin{pmatrix}\omega_x\\ \omega_y\\ \omega_z\end{pmatrix} = \frac{\mu_{\rm B}}{\hbar}\begin{pmatrix} g_x & 0 & 0\\ 0 & g_y & 0\\ 0 & 0 & g_z\end{pmatrix}\begin{pmatrix} B\cos\theta\cos\varphi\\ B\cos\theta\sin\varphi\\ B\sin\theta\end{pmatrix} = \frac{\mu_{\rm B}B}{\hbar}\begin{pmatrix} g_x\cos\theta\cos\varphi\\ g_y\cos\theta\sin\varphi\\ g_z\sin\theta\end{pmatrix}. \quad (1)$$

Here φ is the angle of the **B** projection on the xy plane with respect to the x axis (see the inset in Fig. 5(a)) and g_x, g_y and g_z are the diagonal elements of the g-factor tensor in the selected basis of axes coinciding with the symmetry axes of the QDs. Since the orientation of the magnetic field vector **B** is varied in the xz plane $\varphi = 0$, and the g factor modulus is

$$|g| = \frac{\hbar}{\mu_{\rm B}B}\omega = \sqrt{(g_x\cos\theta)^2 + (g_z\sin\theta)^2}. \quad (2)$$

The lines in Fig. 2(a) show the fits to the experimental data using Eq. (2) for electrons and holes. From these fits we obtain the x and z components of the electron g factor, $|g_{{\rm e},x}| = 1.63$, and $|g_{{\rm e},z}| = 2.52$, as well as the corresponding hole g factors $|g_{{\rm h},x}| = 0.64$, and $|g_{{\rm h},z}| = 2.29$.

The dependence of the oscillation amplitude on θ [Fig. 2(b)] can be modeled by calculating the projection of the rotating spin component on the z axis, as illustrated in Fig. 3 [10]. The optically generated spin polarization is directed along the pump beam (z axis). It rotates about $\boldsymbol{\omega}$, which is inclined with respect to the sample plane xy by the angle $\alpha = \arctan(\omega_z/\omega_x) = \arctan(\tan\theta g_z/g_x)$ [see Eq. (1)]. So, the component of the spin polarization **S** rotating about $\boldsymbol{\omega}$ is $S\cos\alpha$. However, we detect only the projection of this rotating component on the probe beam (z axis) which is given by

$$S_{\rm osc} = S\cos^2\alpha = \frac{S}{1+\tan^2\theta g_z^2/g_x^2}. \quad (3)$$

The projection of the nonoscillating component on the probe direction is

$$S_{\rm no} = S\sin^2\alpha = \frac{S}{1+\cot^2\theta g_x^2/g_z^2}. \quad (4)$$

Note, that $S_{\rm osc} + S_{\rm no} = S$.

According to Eqs. (3) and (4) $S_{\rm osc}$ decreases, while $S_{\rm no}$ increases with θ in agreement with the behavior shown in Fig. 1. Indeed, Eq. (3) gives a good fit to the measured dependence of the oscillation amplitudes on θ as shown in Fig. 2(b). In the fits we use the $|g_x|$ and $|g_z|$ determined from the data in Fig. 2(a). It turns out that a better fit is obtained for θ shifted by $\approx 2^{\rm o}$, which is explained by the nonzero incidence angle ($1^{\rm o} - 2^{\rm o}$) of the probe beam with respect to the growth axis, in order to suppress the influence of scattered light from the degenerate pump.

To explain the dependence of the spin dephasing times T_2^* on θ [Fig. 2(c)] we note that T_2^* at $B \gtrsim 1$ T for these QDs is mostly determined by the inhomogeneous spread, Δg, of the g factor in the QD ensemble [8], especially since we use laser pulses with 10-meV spectral width. The ellipticity signal is proportional to $\int_{-\infty}^{\infty}\cos(g\mu_{\rm B}Bt/\hbar)F(g-g_0)dg$, where F is the distribution function of the g factor in the optically excited ensemble. In the case of a Lorentzian distribution, integration gives oscillations with an exponential decay $\cos(g_0\mu_{\rm B}Bt/\hbar)\exp(-t/T_2^*)$. In the case of a Gaussian distribution, integration gives oscillations with a Gaussian decay $\cos(g_0\mu_{\rm B}Bt/\hbar)\exp(-t^2/2T_2^{*2})$. Note, that for the studied samples both forms of the oscillating function give similar parameters when fitted to the experimental data [8]. The spin dephasing time is given by

$$\frac{1}{T_2^*} = \frac{\Delta g\mu_{\rm B}B}{\hbar}, \quad (5)$$

where the g-factor spread Δg is equal to the half width at half maximum (HWHM) of the Lorentzian distribution or the dispersion of the Gaussian distribution. The x, y, and z components of the g-factor tensor have different spreads (Δg_x, Δg_y, and Δg_z). The ellipticity signal for arbitrary magnetic field orientation in the xz plane is proportional to $\int_{-\infty}^{\infty}\int_{-\infty}^{\infty}\cos\{[g_0 + (g_x - g_{0x})\partial g/\partial g_x + (g_z - g_{0z})\partial g/\partial g_z]\mu_{\rm B}Bt/\hbar\}F_x(g_x - g_{0x})F_z(g_z - g_{0z})dg_x dg_z$ leading to the decaying oscillatory forms described above, with T_2^* given by Eq. (5), where the g-factor spreads for the Lorentzian g-factor distributions F_x and F_z are:

$$\Delta g_{\rm L} = \left|\frac{\partial g}{\partial g_x}\right|\Delta g_x + \left|\frac{\partial g}{\partial g_z}\right|\Delta g_z. \quad (6)$$

For the Gaussian distributions, these spreads are given by:

$$\Delta g_{\rm G} = \sqrt{\left(\frac{\partial g}{\partial g_x}\Delta g_x\right)^2 + \left(\frac{\partial g}{\partial g_z}\Delta g_z\right)^2}, \qquad (7)$$

From Eqs. (2), (5) and Eqs. (6-7) one obtains the dephasing times for the Lorentzian and Gaussian distributions, respectively:

$$T^*_{2,\rm L} = \frac{\hbar}{\mu_{\rm B} B}\cdot\frac{\sqrt{g_x^2\cos^2\theta + g_z^2\sin^2\theta}}{|g_x|\Delta g_x\cos^2\theta + |g_z|\Delta g_z\sin^2\theta}, \qquad (8)$$

$$T^*_{2,\rm G} = \frac{\hbar}{\mu_{\rm B} B}\cdot\frac{\sqrt{g_x^2\cos^2\theta + g_z^2\sin^2\theta}}{\sqrt{(g_x\Delta g_x\cos^2\theta)^2 + (g_z\Delta g_z\sin^2\theta)^2}}. \qquad (9)$$

The solid line in Fig. 2(c) shows fit to the experimental data with Eq. (8). In the fit we use the $|g_x|$ and $|g_z|$ determined from the data in Fig. 2(a); only Δg_x and Δg_z are taken as variables. We obtain the values $\Delta g_{{\rm e},x} = 0.04$, $\Delta g_{{\rm e},z} = 0.09$ for the electron and $\Delta g_{{\rm h},x} = 0.08$, $\Delta g_{{\rm h},z} = 0.27$ for the hole spins. We have also determined the T_2^* and fitted $T_2^*(\theta)$ in the Gaussian approach (not shown). The Gaussian approach gives slightly poorer agreement (at least for electrons) compared to that in the Lorenzian approach, but almost the same $\Delta g_{{\rm e},x}$ and $\Delta g_{{\rm h},x}$. While the $\Delta g_{{\rm e},z}$ and $\Delta g_{{\rm h},z}$ are about 1.2 times larger than the corresponding parameters for the Lorentzian fit, corresponding to an even larger Δg anisotropy.

Figure 4 compares the anisotropies of the electron and hole g factors given by Eq. (2) and their spread given by Eq. (6) in the Lorentzian approach for the parameters determined from the fits in Fig. 2. Interestingly, the anisotropy of electron Δg is somewhat larger than that of g.

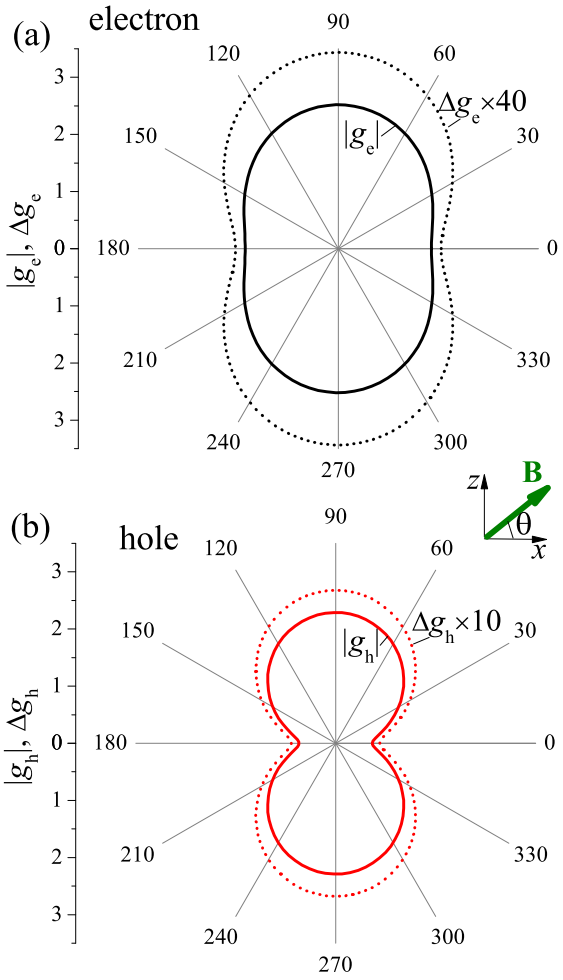

FIG. 4. Dependence of the g-factor moduli (solid lines) and their spreads Δg (dotted lines) for electrons (a) and holes (b) on the angle θ between the sample surface and the magnetic field. The dependencies are given by Eqs. (2) and (6) parametrized with the $|g_x|$, $|g_z|$ and Δg_x, Δg_z that are determined from the experimental data for sample A. The values of Δg are multiplied by factors of 40 and 10 for electrons and holes, respectively, for better visibility.

B. In-plane anisotropy

We also address the in-plane anisotropy of the spin precession by changing the magnetic field vector **B** orientation in the sample plane xy. Figure 5(a) shows the dynamics of the ellipticity signal for different angles φ of **B** with respect to the x axis. Varying φ from 0° to 90° the amplitude and spin dephasing time remain almost unchanged, while the precession frequency slightly decreases. Figure 5(b) shows the g-factor dependencies on φ for electrons and holes. The solid lines show fits to the experimental data with equation

$$|g| = \sqrt{(g_x\cos\varphi)^2 + (g_y\sin\varphi)^2}, \qquad (10)$$

obtained from Eq. (1) for $\theta = 0^{\rm o}$. From the fits we obtain $|g_{{\rm e},x}| = 1.63$, $|g_{{\rm e},y}| = 1.49$ for the electrons and $|g_{{\rm h},x}| = |g_{{\rm h},y}| = 0.64$ for the holes. Surprisingly, for the holes with their complex band structure the in-plane anisotropy vanishes within the experimental accuracy. The electrons on the other hand show a small in-plane anisotropy. From the spin dephasing time at $\varphi = 90^{\rm o}$ we evaluate the g-factor spreads along the y axis: $\Delta g_{{\rm e},y} = 0.04$ and $\Delta g_{{\rm h},y} = 0.07$.

C. Energy dependence

We also studied the electron and hole spin precession for different orientations of the magnetic field in the sample B with a laser energy of 0.79 eV close to the mean energy of the ground-state transition. Figure 6 compares

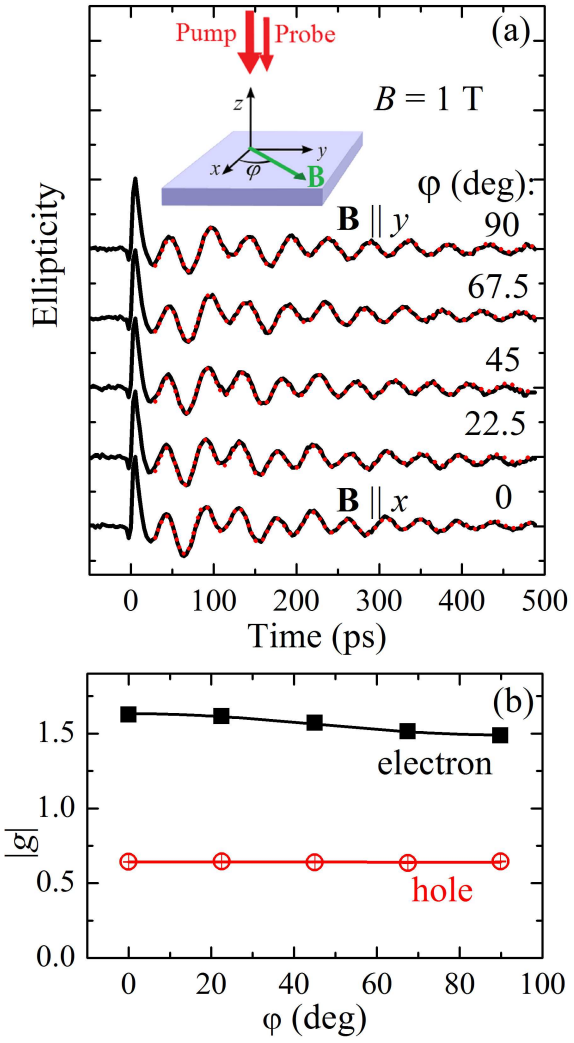

FIG. 5. (a) Dynamics of the ellipticity signal for the magnetic field **B** orientation varied in the sample xy plane, described by different angles φ. The curves are shifted vertically for clarity. Red dotted lines show fits to the experimental data. (b) Dependence of the g-factor moduli on the angle φ for the electrons (solid squares) and holes (open circles). Solid lines show fits to the experimental data with Eq. (10). The data are shown for the sample A at $B = 1$ T and $T = 12$ K. The laser photon energy is set to 0.82 eV. Inset shows the experimental geometry.

the out-of-plane g-factor anisotropies for the two samples A and B. The g_e anisotropy remains almost unchanged at the decreased transition energy [Fig. 6(a)]: The g factor increases by about 13% for the in-plane direction and the direction normal to it. On the other hand, the g_h anisotropy is strongly enhanced with the energy decrease: $|g_{h,x}|$ decreases slightly, but $|g_{h,z}|$ increases strongly from 2.29 up to 3.40. For the sample B, the in-plane g-factor anisotropy stays small with $|g_{e,x}| = 1.90$, $|g_{e,y}| = 1.69$ and $|g_{h,x}| = 0.63$, $|g_{h,y}| = 0.58$. The main g-factor results for both samples are summarized in Table I.

	Electron		Hole	
	0.79 eV	0.82 eV	0.79 eV	0.82 eV
$\|g_x\|$	1.90	1.63	0.63	0.64
$\|g_y\|$	1.69	1.49	0.58	0.64
$\|g_z\|$	2.85	2.52	3.40	2.29
Δg_x		0.04		0.08
Δg_y		0.04		0.07
Δg_z		0.09		0.27
$T_2^*(B = 1\text{ T}, \theta = 0°)$		230 ps		140 ps
$T_2^*(B = 1\text{ T}, \theta = 30°)$		200 ps		50 ps

TABLE I. Components of the electron and hole g-factor tensors and their spreads along the x, y, and z axes for the two transition energies of 0.79 and 0.82 eV in the samples B and A, respectively. The spin dephasing times at $B = 1$ T for $\theta = 0°$ and 30° are also given.

The energy dependencies of the electron and hole g factors are shown in Fig. 7. The solid and open symbols show the transverse ($g_{e,\perp} \equiv g_{e,x}$) and longitudinal ($g_{e,\parallel} \equiv g_{e,z}$) g factors, respectively. The data shown by squares are taken from sample A, and the data shown by triangles from sample B. We take the sign of the electron g factor to be negative, based on previous measurements of the dynamic nuclear polarization in (In,Ga)As/GaAs QDs emitting at larger energies [16]. The correctness of the electron g-factor sign is further confirmed by the fact that both transverse and longitudinal electron g factors increase with energy following the expected trend, see Fig. 7(a): Increase of the electron g factor with energy was also reported in a number of papers on QDs [2, 31], in agreement with the Roth-Lax-Zwerdling relation for bulk semiconductors [4]:

$$g_e(E_g) = g_0 - \frac{2E_p\Delta_{SO}}{3E_g(E_g + \Delta_{SO})}. \qquad (11)$$

Corresponding calculations are shown in Fig. 7(a) by the solid line as function of the band gap energy E_g [8]. As material parameters we use a spin-orbit splitting $\Delta_{SO} = 0.374$ eV of the valence band and a Kane energy $E_p = 24.0$ eV, obtained by linear interpolation between the InAs and GaAs parameters using an average band gap energy $E_g = 0.8$ eV. We added $g_{remote} = -0.13$ to the calculated g factor to account for the contribution from the remote bands [6, 7].

It is instructive to compare Δg evaluated from the spin dephasing time (Table I) with $\Delta g_E = |\partial g/\partial E|\Delta E/2$ from the g-factor dispersion $g(E)$ and the spectral width of the laser $\Delta E = 10$ meV used in the experiments where corresponding dephasing time was determined. The factor 1/2 arises from the definition of Δg as HWHM of the g-factor distribution. This comparison is shown in Table II for the x and z directions. $\Delta g_E \gtrsim \Delta g/2$ except of $\Delta g_{h,x}$. Thus, the g-factor dispersion accounts for

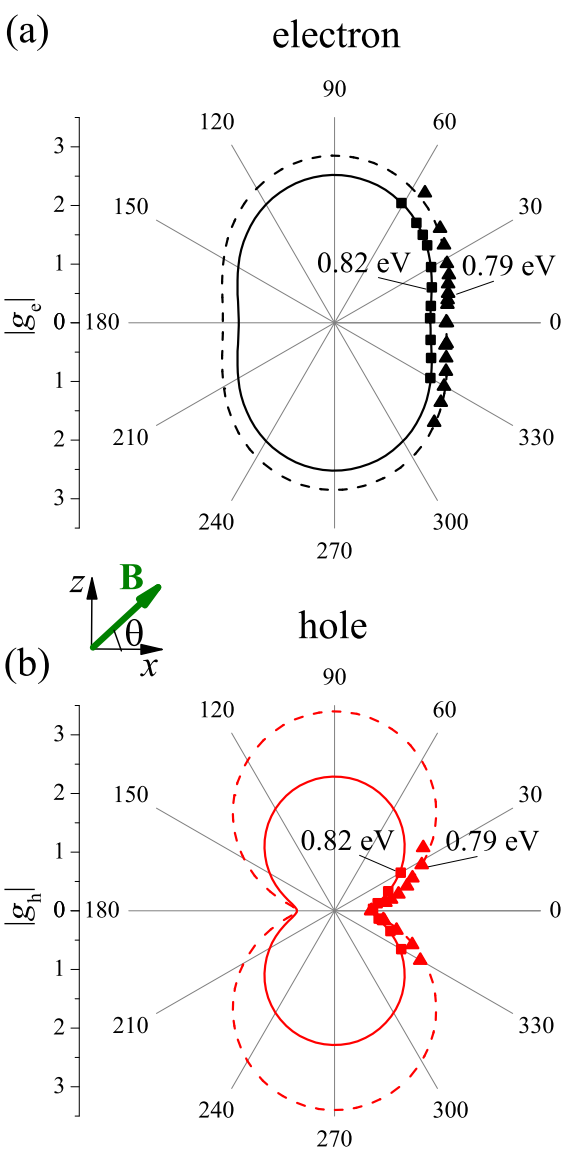

FIG. 6. Dependence of the g-factor moduli for electrons (a) and holes (b) on the angle θ between the sample surface and the magnetic field for the samples A (squares, 0.82 eV transition energy) and B (triangles, 0.79 eV). Lines show fits to the experimental data with Eq. (2).

	Δg_x	Δg_{xE}	Δg_z	Δg_{zE}
Electron	0.04	0.03	0.09	0.05
Hole	0.08	0.02	0.27	0.15

TABLE II. Comparison of the g-factor spreads Δg along the x and z axes, evaluated on one hand from the spin dephasing time and on the other hand from the g-factor dispersion at 0.82 eV energy and laser spectral width $\Delta E = 10$ meV for sample A.

a significant part of Δg. Indeed, measurements with a smaller laser spectral width $\Delta E = 5$ meV on sample A give $\Delta g_{e,x} \approx 0.03$ and $\Delta g_{h,x} \approx 0.07$, smaller than those measured for $\Delta E = 10$ meV.

Let us turn to the electron g-factor dispersions shown in Fig. 7(a). The large difference between the transverse and longitudinal g factors, $\delta g = g_{e\perp} - g_{e\|} \sim 1$, indicates that at the small band-gap energies E_g, for strong confinement, the electron g factor is strongly affected by the directional variations of the QDs, e.g., in strain and in size, as they have a diameter of ~ 45 nm and a height of ~ 10 nm. Indeed, electron g-factor anisotropy is dominated by the hole confinement, and, e.g., in QWs δg is proportional to the difference of light- and heavy-hole energies [5, 32]. Note, that in (In,Ga)As/GaAs QDs emitting around 1.4 eV and having comparable height-to-diameter ratio, but much smaller confinement, the g_e anisotropy is much smaller ($\delta g_e \sim 0.1$) [15, 16]. Also, small is the g_e deviation from the Roth-Lax-Zwerdling relation.

Our observation of a large electron g-factor anisotropy is qualitatively confirmed by the model of Ref. [7]. The dashed and dotted lines in Fig. 7(a) show the calculated energy dependencies of the transverse and longitudinal electron g factors, $g_{e\perp}$ and $g_{e||}$, respectively, for a QW. The QW approximation of the model [7] is reasonable for the studied dome-shaped QDs, since their diameter is much larger than their height. The calculation details and used parameters can be found in Refs. [7] and [8], respectively. The calculations give approximately the same difference $g_{e\perp}(E) - g_{e||}(E)$ as observed in experiment. However, there is some deviation between experiment and calculations in the absolute g-factor values. A more refined theoretical description of electron g factors taking into account effects of strain, composition etc is still needed to reach quantitative agreement with the experimental data.

We also calculate the longitudinal g factor for holes, $g_{h||}$, in the framework of the numerical method developed in Refs. [33, 34]. The quantum dots are modeled as disks with Gaussian potential profiles for electrons and holes $V_{e(h)}$:

$$V_{e(h)}(r,z) = V_{c(v)}\left(1 - \exp\left[-\frac{4r^2}{D^2} - \frac{4z^2}{H^2}\right]\right). \qquad (12)$$

Here $V_{c(v)}$ is the conduction (valence) band discontinuity between QD and barrier, D and H are the QD effective diameter and height, respectively. The ratio $V_c : V_v$ is taken as 6 : 4. The QD composition is assumed to be gradually varying between the QD center, $In_pAl_qGa_qAs$, $p + 2q = 1$, and the barrier, $In_{0.53}Al_{0.24}Ga_{0.23}As$. The dependence of the band gap on the composition is taken from Ref. [35]. Other band structure parameters are linearly interpolated between the corresponding values of pure InAs, AlAs and GaAs also taken from [35]. Calculations show that the $g_{h||}$ is determined by the height-to-diameter ratio of the QDs, H/D, and to less extent by the QD composition. On the other hand, the QD emission

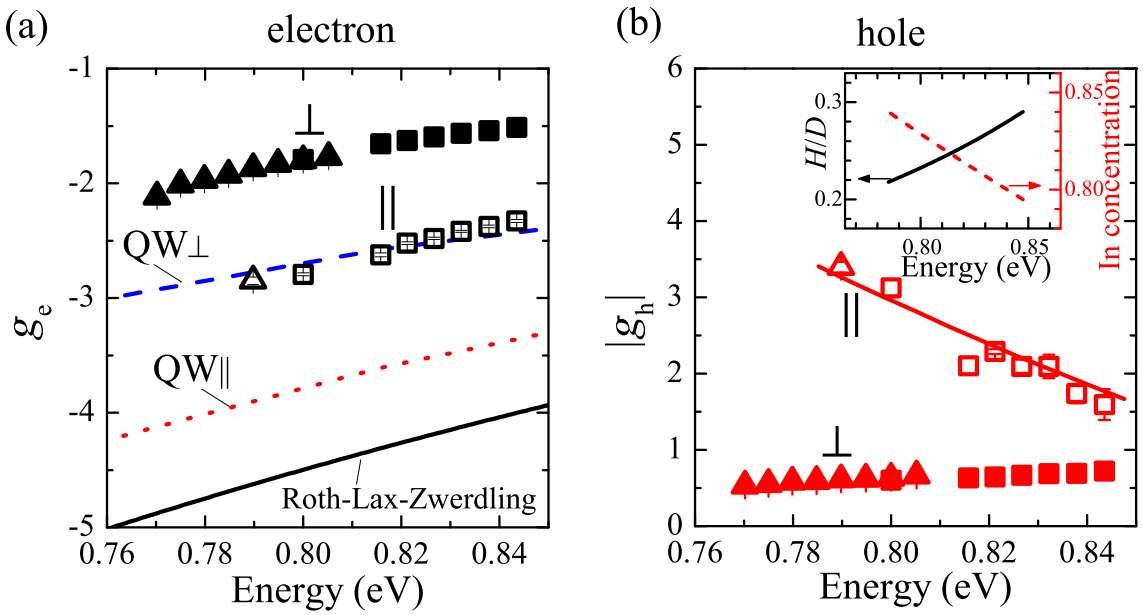

FIG. 7. Dependence of the electron (a) and hole (b) g factors on the central laser photon energy. The solid and open symbols show the transverse and longitudinal g factors, respectively. The data corresponding to samples A and B are shown by squares and triangles, respectively. The solid line in panel (a) shows the expected dependence for bulk semiconductors calculated according to the Roth-Lax-Zwerdling relation (11). The dashed and dotted lines in panel (a) show the transverse and longitudinal g-factor dependencies, respectively, calculated for QWs using the model of Ref. [7]. In panel (b) the solid line shows the calculated longitudinal hole g factor using the model of Refs. [33, 34]. Inset shows the corresponding calculated dependencies of the height-to-diameter ratio (solid line, left axis) and the indium content (dashed line, right axis) on the QD emission energy.

energy is more strongly affected by the QD composition than by the QD size. The solid line in Fig. 7(b) shows the calculated dependence for $H = 11$ nm, D varied from 50 to 38 nm, and the Indium content in the QD center varied from 0.84 to 0.80. The corresponding dependencies on the H/D ratio (solid line, left axis) and In content (dashed line, right axis) on the QD emission energy are shown in the inset of Fig. 7(b). Thus, with increasing QD emission energy the H/D increases and the In concentration decreases.

IV. CONCLUSIONS

By implementing a vector magnet into a setup for time-resolved pump-probe ellipticity studies, we performed a detailed study of the g-factor anisotropy of electrons and holes in InAs/$In_{0.53}Al_{0.24}Ga_{0.23}As$ self-assembled quantum dots, emitting in the telecom spectral range around 0.8 eV. All components of the g-factor tensors were measured, as well as their spreads in the QD ensemble. The electron g factor shows a comparatively huge out-of-plane anisotropy changing from $g_{e,x} = -1.63$ to $g_{e,z} = -2.52$ at a transition energy of 0.82 eV. The hole g-factor anisotropy at this energy is even stronger: $|g_{h,x}| = 0.64$ and $|g_{h,z}| = 2.29$. It increases even further at a smaller transition energy of 0.79 eV: $|g_{h,x}| = 0.63$ and $|g_{h,z}| = 3.40$. The spread of the g factors determined from the spin dephasing time shows a pronounced out-of-plane anisotropy, both for electrons and holes. On the other hand, the in-plane anisotropy of the electron and hole g factors is small. The energy dependence of the longitudinal hole g factors has been described applying the theoretical model of Refs. [33, 34], which has allowed us to estimate the QD parameters: size and composition. In particular, it is shown that with increasing emission energy, the height-to-diameter ratio of the QDs increases while the indium content in QD decreases.

ACKNOWLEDGMENTS

We are grateful to A. Greilich, E. L. Ivchenko, A. A. Kiselev and I. A. Yugova for valuable advices and useful discussions. We acknowledge the financial support by the Russian Science Foundation (Grant No. 14-42-00015), the Deutsche Forschungsgemeinschaft in the frame of the ICRC TRR 160, as well as by BMBF in the frame of the project Q.com-H (Contracts No. 16KIS0112 and No. 16KIS0104K).

[1] A. V. Khaetskii and Y. V. Nazarov, Spin relaxation in semiconductor quantum dots, Phys. Rev. B **61**, 12639 (2000).

[2] A. Greilich, D. R. Yakovlev, A. Shabaev, Al. L. Efros, I. A. Yugova, R. Oulton, V. Stavarache, D. Reuter, A. Wieck, and M. Bayer, Mode locking of electron spin coherences in singly charged quantum dots, Science **313**, 341 (2006).

[3] F. Henneberger and O. Benson, eds., *Semiconductor Quantum Bits* (Pan Stanford, Singapore, 2008).

[4] L. M. Roth, B. Lax, and S. Zwerdling, Theory of optical magneto-absorption effects in semiconductors, Phys. Rev. **114**, 90 (1959).

[5] A. A. Sirenko, T. Ruf, M. Cardona, D. R. Yakovlev, W. Ossau, A. Waag, and G. Landwehr, Electron and hole g factors measured by spin-flip Raman scattering in $CdTe/Cd_{1-x}Mg_xTe$ single quantum wells, Phys. Rev. B **56**, 2114 (1997).

[6] I. A. Yugova, A. Greilich, D. R. Yakovlev, A. A. Kiselev, M. Bayer, V. V. Petrov, Yu. K. Dolgikh, D. Reuter, and A. D. Wieck, Universal behavior of the electron g-factor in GaAs/AlGaAs quantum wells, Phys. Rev. B **75**, 245302 (2007).

[7] A. A. Kiselev, E. L. Ivchenko, and U. Rössler, Electron g factor in one- and zero-dimensional semiconductor nanostructures, Phys. Rev. B **58**, 16353 (1998).

[8] V. V. Belykh, A. Greilich, D. R. Yakovlev, M. Yacob, J. P. Reithmaier, M. Benyoucef, and M. Bayer, Electron and hole g factors in InAs/InAlGaAs self-assembled quantum dots emitting at telecom wavelengths, Phys. Rev. B **92**, 165307 (2015).

[9] J. Hübner, S. Kunz, S. Oertel, D. Schuh, M. Pochwala, H. T. Duc, J. Förstner, T. Meier, and M. Oestreich, Electron g-factor anisotropy in symmetric (110)-oriented GaAs quantum wells, Phys. Rev. B **84**, 041301 (2011).

[10] G. Salis, D. D. Awschalom, Y. Ohno, and H. Ohno, Origin of enhanced dynamic nuclear polarization and all-optical nuclear magnetic resonance in GaAs quantum wells, Phys. Rev. B **64**, 195304 (2001).

[11] A. Malinowski and R. T. Harley, Anisotropy of the electron g factor in lattice-matched and strained-layer III-V quantum wells, Phys. Rev. B **62**, 2051 (2000).

[12] Yu. A. Nefyodov, A. V. Shchepetilnikov, I. V. Kukushkin, W. Dietsche, and S. Schmult, g-factor anisotropy in a $GaAs/Al_xGa_{1-x}As$ quantum well probed by electron spin resonance, Phys. Rev. B **83**, 041307 (2011).

[13] Yu. A. Nefyodov, A. V. Shchepetilnikov, I. V. Kukushkin, W. Dietsche, and S. Schmult, Electron g-factor anisotropy in $GaAs/Al_{1-x}Ga_xAs$ quantum wells of different symmetry, Phys. Rev. B **84**, 233302 (2011).

[14] P. Le Jeune, D. Robart, X. Marie, T. Amand, M. Brousseau, J. Barrau, V. Kalevich, and D. Rodichev, Anisotropy of the electron Landé g factor in quantum wells, Semicond. Sci. Technol. **12**, 380 (1997).

[15] A. Schwan, B. M. Meiners, A. Greilich, D. R. Yakovlev, M. Bayer, A. D. B. Maia, A. A. Quivy, and A. B. Henriques, Anisotropy of electron and hole g-factors in (In,Ga)As quantum dots, Appl. Phys. Lett. **99**, 221914 (2011).

[16] I. A. Yugova, A. Greilich, E. A. Zhukov, D. R. Yakovlev, M. Bayer, D. Reuter, and A. D. Wieck, Exciton fine structure in InGaAs/GaAs quantum dots revisited by pump-probe Faraday rotation, Phys. Rev. B **75**, 195325 (2007).

[17] J. M. Meyer, I. Hapke-Wurst, U. Zeitler, R.J. Haug, and K. Pierz, Resonant tunnelling through InAs quantum dots in tilted magnetic fields: experimental determination of the g-factor anisotropy, Phys. Status Solidi B **224**, 685 (2001).

[18] T. P. Mayer Alegre, F. G. G. Hernández, A. L. C. Pereira, and G. Medeiros-Ribeiro, Landé g tensor in semiconductor nanostructures, Phys. Rev. Lett. **97**, 236402 (2006).

[19] J. van Bree, A. Yu. Silov, M. L. van Maasakkers, C. E. Pryor, M. E. Flatté, and P. M. Koenraad, Anisotropy of electron and hole g tensors of quantum dots: An intuitive picture based on spin-correlated orbital currents, Phys. Rev. B **93**, 035311 (2016).

[20] I. Hapke-Wurst, U. Zeitler, R.J. Haug, and K. Pierz, Mapping the g factor anisotropy of InAs self-assembled quantum dots, Physica E (Amsterdam) **12**, 802 (2002).

[21] S. A. Crooker, J. Brandt, C. Sandfort, A. Greilich, D. R. Yakovlev, D. Reuter, A. D. Wieck, and M. Bayer, Spin noise of electrons and holes in self-assembled quantum dots, Phys. Rev. Lett. **104**, 036601 (2010).

[22] C. Gradl, M. Kempf, D. Schuh, D. Bougeard, R. Winkler, C. Schüller, and T. Korn, Hole-spin dynamics and hole g-factor anisotropy in coupled quantum well systems, Phys. Rev. B **90**, 165439 (2014).

[23] D. N. Krizhanovskii, A. Ebbens, A. I. Tartakovskii, F. Pulizzi, T. Wright, M. S. Skolnick, and M. Hopkinson, Individual neutral and charged $In_xGa_{1x}AsGaAs$ quantum dots with strong in-plane optical anisotropy, Phys. Rev. B **72**, 161312 (2005).

[24] A. V. Koudinov, I. A. Akimov, Yu. G. Kusrayev, and F. Henneberger, Optical and magnetic anisotropies of the hole states in Stranski-Krastanov quantum dots, Phys. Rev. B **70**, 241305 (2004).

[25] E. A. Zhukov, D. R. Yakovlev, A. Schwan, O. A. Yugov, A. Waag, L. W. Molenkamp, and M. Bayer, Spin coherence of electrons and holes in ZnSe-based quantum wells studied by pump-probe Kerr rotation, Phys. Status Solidi B **251**, 1872 (2014).

[26] J. Krauth, A. Steinmann, R. Hegenbarth, M. Conforti, and H. Giessen, Broadly tunable femtosecond near- and mid-IR source by direct pumping of an OPA with a 41.7 MHz Yb:KGW oscillator, Opt. Express **21**, 11516 (2013).

[27] M. M. Glazov, I. A. Yugova, S. Spatzek, A. Schwan, S. Varwig, D. R. Yakovlev, D. Reuter, A. D. Wieck, and M. Bayer, Hole-spin dynamics and hole g-factor anisotropy in coupled quantum well systems, Phys. Rev. B **82**, 155325 (2010).

[28] S. Varwig, A. Schwan, D. Barmscheid, C. Müller, A. Greilich, I. A. Yugova, D. R. Yakovlev, D. Reuter, A. D. Wieck, and M. Bayer, Hole spin precession in a (In,Ga)As quantum dot ensemble: From resonant spin amplification to spin mode locking, Phys. Rev. B **86**, 075321 (2012).

[29] D. R. Yakovlev and M. Bayer, Coherent spin dynamics of carriers, in *Spin Physics in Semiconductors*, edited by M. I. Dyakonov (Springer, Berlin, 2008) Chap. 6, pp. 135–177.

[30] M. Kroutvar, Y. Ducommun, D. Heiss, M. Bichler, D. Schuh, G. Abstreiter, and J. J. Finley, Optically programmable electron spin memory using semiconductor quantum dots, Nature **432**, 81 (2004).

[31] A. Schwan, B.-M. Meiners, A. B. Henriques, A. D. B. Maia, A. A. Quivy, S. Spatzek, S. Varwig, D. R. Yakovlev, and M. Bayer, Dispersion of electron g-factor with optical transition energy in (In,Ga)As/GaAs self-assembled quantum dots, Appl. Phys. Lett. **98**, 233102 (2011).

[32] E. L. Ivchenko, *Optical Spectroscopy of Semiconductor Nanostructures* (Alpha Science International, Harrow, 2005) p. 241.

[33] M. A. Semina and R. A. Suris, Holes localized in nanostructures in an external magnetic field: g-factor and mixing of states, Semiconductors **49**, 797 (2015).

[34] M. A. Semina, A. A. Golovatenko, and A. V. Rodina, Ground state of the holes localized in II-VI quantum dots with Gaussian potential profiles, Phys. Rev. B **93**, 045409 (2016).

[35] I. Vurgaftman, J. R. Meyer, and L. R. Ram-Mohan, Band parameters for III-V compound semiconductors and their alloys, J. Appl. Phys. **89**, 5815 (2001).